applied sciences

MDPI

Article

Characterizing Crustal Deformation of the Weihe Fault, Weihe Basin (Central China), Using InSAR and GNSS Observations

Qin-Hu Tian [1], Wen-Ting Zhang [2,3,*] and Wu Zhu [3,4]

[1] Shaanxi Earthquake Agency, Xi'an 710068, China; glorich@126.com
[2] Second Monitoring and Application Center, CEA, Xi'an 710054, China
[3] Key Laboratory of Ecological Geology and Disaster Prevention, Ministry of Natural Resources, Xi'an 710054, China; zhuwu@chd.edu.cn
[4] College of Geology Engineering and Geomatics, Chang'an University, Xi'an 710064, China
* Correspondence: wt_zhang93@163.com; Tel.: +86-29-85506645

Abstract: The Weihe Fault is an important basement fault that is buried deep and controls the formation, evolution, and seismicity of the Weihe Basin. It has been quiescent for more than 300 years with only a few moderate and small earthquakes distributed unevenly. Therefore, it is necessary to investigate the current tectonic deformation pattern in order to assess regional seismic risk. In this context, the tectonic deformation velocities of the Weihe Fault were analyzed using an interferometric synthetic aperture radar (InSAR), a global navigation satellite system (GNSS) and leveling observations. The line of slight (LOS) deformation rates spanning from 2015 to 2019 were estimated from stacking-InSAR technology. Subsequently, the three-dimensional deformation rates in the north–south, east–west, and vertical directions were separated through the integration of GNSS-derived horizontal deformation and InSAR-derived LOS deformation. After that, the long-wavelength tectonic deformation was decomposed from the separated vertical deformation based on the spherical wavelet multiscale approach. Finally, the slip rate and locking depth were inverted for the assessment of the seismic hazard and tectonic activity of the Weihe Fault. The results show that the separated vertical deformation is consistent with the leveling observations, where the standard deviation between them is 1.69 mm/yr and the mean value is 0.6 mm/yr, demonstrating the reliability of the proposed method. The decomposed long-wavelength tectonic deformation exhibits uplift in the north and subsidence in the south, as well as the obvious vertical velocity gradient. The inversion result shows that the slip rate of the Weihe Fault gradually decreases from the west to the east, and the dip gradually increases from the west to the east, indicating a segmented activity and the geometric characteristics of the fault. The locking depth of the Weihe Fault gradually increases from the west (~5 km) to the east (~14 km), implying a higher stress accumulation and seismic risk on the eastern section of the fault. Taking into account the higher locking depth and frequent historical earthquakes on the eastern section of the Weihe Fault, further attention should be paid to the earthquake risk of the eastern section of the Weihe Fault.

Keywords: Weihe Fault; crustal deformation; InSAR; GNSS

check for updates

Citation: Tian, Q.-H.; Zhang, W.-T.; Zhu, W. Characterizing Crustal Deformation of the Weihe Fault, Weihe Basin (Central China), Using InSAR and GNSS Observations. *Appl. Sci.* **2023**, *13*, 6835. https://doi.org/10.3390/app13116835

Academic Editor: Edoardo Rotigliano

Received: 7 May 2023
Revised: 27 May 2023
Accepted: 2 June 2023
Published: 5 June 2023

1. Introduction

The Weihe Basin is an intracontinental basin characterized by shear tensile deformation and strong tectonic activity [1]. The fault's depression pattern has been formed since the Eocene under the influence of regional tectonic horizontal extension and vertical force generated by deep material movement. Quaternary active normal faults are well-developed in the Weihe Basin and divided it into multiple fault blocks [2]. The fault structures are dominated by deep and large fault zones in the near EW direction, as well as some secondary NW and NE directions, which jointly control the structural pattern and earthquake-breeding of the Weihe Basin [3]. Among them, the Weihe Fault shows the most significant segmentation to the basin, with 68% of earthquakes above magnitude 4 and about 70% of earthquakes above magnitude 5 since 1177 AD [4]. In particular, the M8.0 earthquake in Huaxian County, Shaanxi Province on 23 January 1556, is the deadliest earthquake event in China's history, causing over 830,000 casualties and huge property losses [5]. The Moho interface uplifted abruptly relative to the Ordos block and high-speed materials from the upper mantle intruded into the lower crust, providing deep structural conditions for moderately strong earthquakes above [6]. However, it has been quiescent for more than 300 years with only a few moderate and small earthquakes distributed unevenly. Therefore, the Weihe Fault has always attracted attention. Crustal deformation is the direct manifestation of deeper fault activity and therefore plays an important role in understanding the current tectonic deformation pattern and in assessing regional seismic risk.

Global navigation satellite system (GNSS) observations are commonly used in the monitoring of the crustal deformation of the Weihe Basin and Fault. The three-dimensional slip rate of the main faults in the Weihe Basin was analyzed through processing GNSS data, combined with the particle swarm algorithm and theoretical dislocation model [7]. The next year, a finite element dynamic model of the Weihe Basin was established to study the characteristics of the regional crustal stress field based on high-precision GNSS monitoring data, and the internal relationship between the Weihe Basin tectonic stress field, and local ground fissures was analyzed [8]. Three-dimensional crustal deformation was derived from GNSS observations before and after the Wenchuan earthquake, and found that the obvious deformation of the Weihe Basin and Fault was caused by strong earthquakes [9]. The tectonic stress and activity characteristics of the faults were inverted by using GNSS, and the genetic mechanism of the earthquakes and ground fissure disasters were subsequently analyzed in the Weihe Basin [10]. The regional vertical motion velocity field was obtained through the dynamic adjustment method constrained by the GNSS vertical motion rate, and the dip-slip rate and locking depth of the main faults were inverted in the Weihe Basin [11]. The Weihe Basin was mainly dominated by extensional movement through GNSS observations, and the differences between the current crustal movement and strain of the Weihe basin and surrounding blocks were analyzed [12]. The maximum shear strain rate at the western end of the Weihe basin appeared in the cycle of 2015–2017, and showed a north–south rotation [13].

As an advanced space observation technology, interferometric synthetic aperture radar (InSAR) has been employed to map the ground deformation of the Weihe Fault. The land subsidence and ground fissure hazards over the Weihe Basin were investigated from InSAR and other technologies, and indicated that the spatial pattern of these hazards was controlled by active faults in the basin, including the Weihe Fault [14]. About 1 mm/yr ground deformation of the Weihe Fault was detected through processing 32 European Space Agency(ESA) Envisat ASAR images from the descending track 161 orbit between 2003 and 2010 [15]. The vertical deformation rate of the Weihe Fault was derived from ascending Sentinel-1A images and descending ALOS-2 ScanSAR images, and the distribution of fault slip was subsequently inverted by using a multi-fault model [16]. The results confirmed the creep characteristics of the Weihe Fault. InSAR ground deformation maps were produced during 2015–2019 using Sentinel-1A/B and ALOS/PALSAR-2 ScanSAR images over the Weihe Basin, where the vertical and east–west deformation components decomposed from ascending and descending InSAR measurements showed that vertical movement dominated the deformation of the Weihe Basin [2]. A slip rate of ~13.7 mm/yr on the Weihe Fault was inverted from the InSAR observations, which explained the phenomenon of uplift along the Weihe Fault.

Although intensive research has been conducted in investigating the tectonic deformation of the Weihe Basin and Weihe Fault, most research is based on independent deformation observation technologies, such as GNSS-derived horizontal deformation, InSAR-derived line of slight (LOS) deformation, and leveling-derived vertical deformation. These independent observations may not reflect the accurate tectonic deformation of the

Weihe Fault in a different temporal-spatial scale. In this context, this study combines the InSAR, GNSS, and leveling data to obtain high-spatial-resolution ground deformation along the Weihe Fault. Subsequently, long-wavelength deformation caused by tectonic movement and small-scale deformation caused by human activities are separated by the spherical wavelet-based multiscale approach. Finally, the fault slip rate and locking depth of the Weihe Fault are inverted from an improved dip-slip model.

2. Study Area and Datasets

2.1. Background of Study Area

The study area is in the Weihe Basin, which is located in the Shaanxi Province in central China and is surrounded by the Qinghai–Tibet Block, Ordos Block, North China Block, and South China Block, as shown in Figure 1. The Yellow River flows through the eastern part of the basin. The Wei River flows from west to east and converges with the Yellow River at Tongguan. The Weihe Basin has a semi-arid climate, which is mainly affected by both the East Asia Summer Monsoon and Winter Monsoon [17]. The precipitation of the basin decreases gradually from the southeast to the northwest [18]. The development of the Weihe Basin was controlled by its southern and northern boundary faults. Five of the most important faults in the Weihe Basin are the Qinling Piedmont Fault (QPF), the Huashan Piedmont Fault (HPF), the Kouzhen-Guanshan Fault (KGF), the Qishan-Mazhao Fault (QMF), and the Weihe Fault (WF) [19], as shown in Figure 1. The QPF bounds the Weihe Basin on the south, building up an approximate EW-trending 210 km long mountain frontal fault. The QPF has the metamorphic rock and granite Qinling Mountains on its upthrown side, as well as the well-dated and thick Cenozoic loess tableland on its downthrown side [2]. The KGF is a hidden fault in the northeastern Weihe Basin, which has an overall strike of EW, a length of 100–150 km, a south dip of 40–80°, and is one of the most seismically active faults in the Weihe Basin [20]. The HPF is an important active fault on the southeast side of the Weihe Basin and has been highly active since the Cenozoic [21]. The QMF is the longest and most active fault in the basin, which bounds the southwestern margin of the Ordos block for more than 100 km [22]. The Weihe Fault is a basement fault zone buried deep along the Wei River, which has a length over 300 km, a width of 1–2 km, and an overall strike of EW. The depth of the Weihe Fault decreases gradually from the west to east.

2.2. Data Collection

To observe the ground deformation rate of the Weihe Fault, the SAR, GNSS, and leveling data were collected. For the SAR data, 26 Sentinel-1A Interferometric Wide Swath (IW) single-look complexes (SLC) spanning from 2015 to 2019 were downloaded from the ESA's Sentinels Scientific Data Hub ("https://scihub.copernicus.eu"(18 December 2022)). The SAR data were processed by the stacking-InSAR technique to obtain the high-spatial-resolution LOS deformation rate from 2015 to 2019. Table 1 shows the parameters of these SAR images. The shuttle radar topography mission (SRTM) digital elevation model (DEM), which had a spatial resolution of 30 m, was acquired as an external DEM to remove the topographic phase from the differential interferograms. The GNSS-derived horizontal deformation rates, with a temporal span of 1999 to 2016, were acquired from the Crustal Movement Observation Network of China (CMONOC) [23], as shown by the blue arrows in Figure 1. The longer time span of GNSS data enabled more accurate velocity estimates. The SAR-derived and GNSS-derived deformation rates were further combined to produce the three-dimensional deformation rates. The leveling-derived deformation rates in the vertical direction were mainly from the network of leveling benchmarks used for seismic applications across the major active faults in China and those surveyed by the China Earthquake Administration (CEA) [24], as shown by the gray arrows in Figure 1. In this study, the leveling deformation rates were mainly used for evaluating the vertical deformation rates produced by the integration of SAR and GNSS.

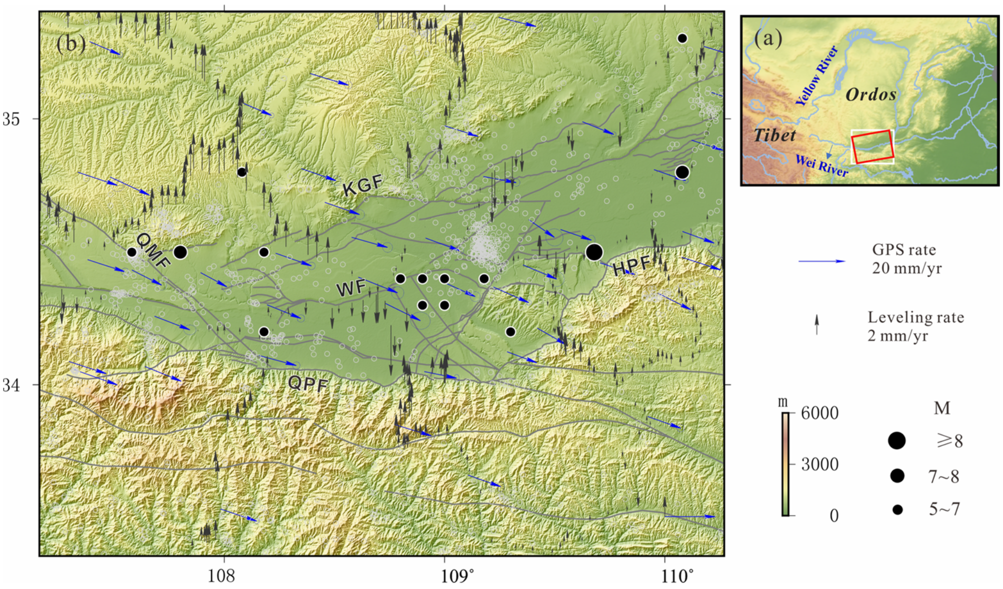

Figure 1. The location of the study area (**a**), where the white and red rectangles show the coverages of the study area and SAR images, respectively; the blue lines show the rivers in the Weihe Basin. The enlarged study area is shown in (**b**), where the gray lines represent the faults in the Weihe Basin; the black circles represent the historic earthquake events above magnitude 5; the white circles represent the historic earthquake events below magnitude 5; the blue arrows represent the GNSS-derived horizontal deformation rates; and the black arrows represent the leveling-derived vertical deformation rate.

Table 1. Data coverage for SAR images used in this study.

Satellite	Path	Orbital Direction	Azimuth Angle	Data Period	No. of Images
Sentinel-1A	84	Ascending	−13	12/2015–03/2019	26

3. Methods

3.1. LOS Deformation Rate Derived from Stacking-InSAR

The collected Sentinel-1A SAR images spanning from 2015 to 2019 were processed by stacking-InSAR technology to obtain the LOS deformation rate. Stacking-InSAR is an enhancement technology that obtains the deformation rate by linearly stacking a set of unwrapped differential interferograms, and is expressed by the following equation [25]:

$$\mathrm{Ph}_{\mathrm{rate}} = \frac{\sum_{j=1}^{N} \Delta t_j \varphi_j}{\sum_{j=1}^{N} \Delta t^2} \tag{1}$$

where $\mathrm{Ph}_{\mathrm{rate}}$ was the deformation rate; N was the number of interferograms involved in the estimation; Δt_j was the time interval between the master and slave image; and φ_j were the unwrapped interferograms. Prior to stacking-InSAR processing, the interferograms with perpendicular baselines shorter than 100 m and temporal baselines longer than 300 days were produced in this study. This operation could mitigate the noise effects and preserved the temporal and spatial coherence characteristics of the interferograms. It should be noted that the temporal baseline threshold of 300 days, which was considered longer than the conventional stacking-InSAR processing, was designed with the purpose of capturing long-term accumulated surface deformation along the Weihe Fault. As a result, 74 interferometric pairs were produced and involved in the deformation rate estimation (Figure 2). The collected SRTM DEM was used to improve co-registration accuracy and correct topographic phase contributions in all interferograms. The process of adaptive spectral filtering with a window size of 32 was executed to suppress interferometric noise [26].

Phase unwrapping of the minimum cost flow (MCF) method was carried out to retrieve the absolute phase [27]. After processing, the unwrapped interferometric phase may have consisted in residual phase errors, such as orbital error and atmospheric delay error. In this case, the atmospheric delay errors, which were highly correlated in space but poorly in time, were mitigated through the cascade of a low-pass filter implemented in the two-dimensional spatial domain, followed by temporal high-pass filtering [28]. This filtering operation also allowed us to detect possible orbital phase errors caused by inaccurate SAR orbital information. It was found that the orbital errors were not obvious for the generated interferograms; therefore, there was no further manipulation with the orbital error. The detection of possible orbital errors was important in monitoring tectonic deformation since both of them presented the characteristic of a long wavelength. The empirical linear model between the interferometric phase and elevation was constructed to mitigate the residual atmospheric errors with respect to terrain. Finally, the LOS deformation rate was obtained from Equation (1).

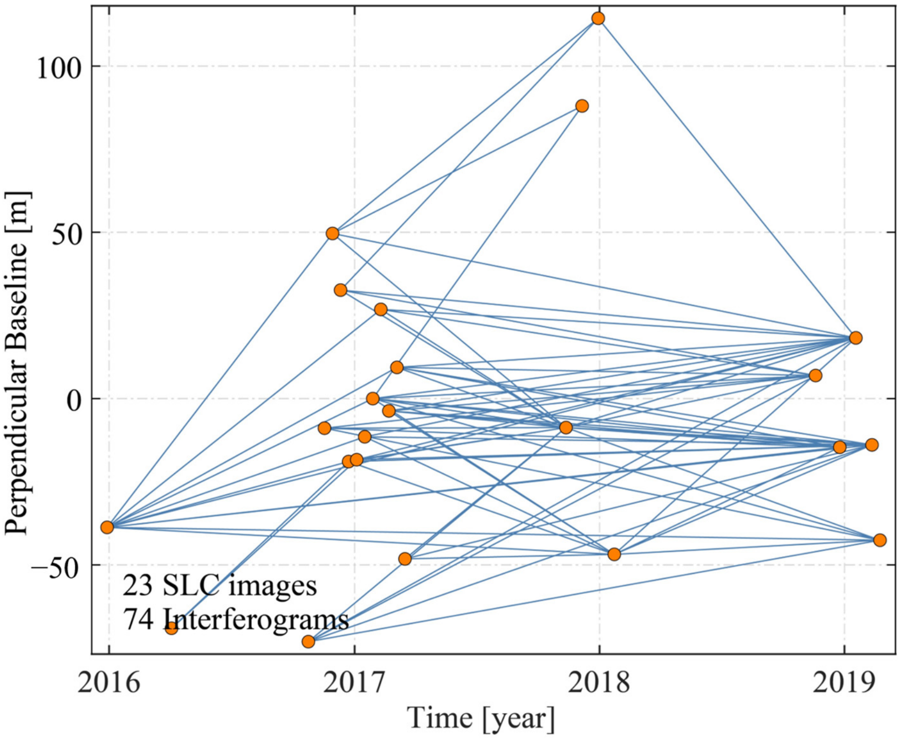

Figure 2. Distribution of temporal and spatial baselines. Orange dots indicate Sentinel-1 acquisitions, and blue lines represent the generated interferograms.

3.2. Three-Dimensional Deformation Rate by Integrating of GNSS and InSAR

Previous studies showed that the Weihe Fault was dominated by vertical deformation and slight strike–slip shear movement [24]. The deformation estimated from stacking-InSAR was in the one-dimensional LOS direction. GNSS observations can measure the two-dimensional horizontal displacements at discrete locations with millimeter-level accuracy. Therefore, this study calculated high-spatial-resolution three-dimensional ground deformation through the integration of InSAR LOS deformation and GNSS horizontal deformation [29].

The software published by [30] was used to calculate the integrated three-dimensional deformation rates, where the north–south rate was mainly constrained by GNSS observation, the east–west rate was constrained by both InSAR and GNSS observations, and the vertical rate was constrained by the InSAR observations. The leveling observation with a more reliable vertical accuracy was not involved in the three-dimensional deformation estimation due to the nonuniform spatial distribution, which may have distorted the overall deformation. The discrete GNSS deformation rates were interpolated to the same grid interval of InSAR observations by utilizing the algorithm proposed by [31], where the GNSS network density and configurations were considered during the process of data weighting. The Gaussian distance weighting function and a Voronoi cell-spatial weighting function were used in the interpolation. The offsets between InSAR and GNSS reference frames were also calculated and removed from the InSAR LOS deformation rate. Finally, the three-dimensional velocity was solved for each grid by combining the GNSS-interpolated velocities and the InSAR LOS velocities through least-squares regression.

3.3. Tectonic Deformation Decomposition through Wavelet Analysis

The studies have indicated that the vertical deformation field along the Weihe Fault occurred at multiple length scales, including long-wavelength deformation caused by tectonic movement and small-scale deformation caused by human activities [2,14]. A scale of tens to hundreds of kilometers might be reasonable for a given tectonic deformation, while a scale of several kilometers might be reasonable for local deformations due to hydrological variations. Therefore, it is necessary to calculate the deformation at different spatial scales to better characterize the fault activities caused by the different mechanisms. In this study, a spherical wavelet-based multiscale approach was used to estimate the spatial velocity field in different scales since any velocity field on the sphere can be represented as a linear combination of spherical wavelets [32]. Different from the physical model, the spherical wavelet-based multiscale approach is a non-physical model, which separates the deformation processes at different spatial scales without imposing physical descriptions of the system. The secular tectonic motion and time-dependent subtle signals were simultaneously detected by selecting different scale factors. Based on the geometric properties of the spherical–triangular grids summarized in Table 2, the scale factor q = 5–10 was used as the secular vertical tectonic deformation field and q = 11–12 was used as the local human-activities-induced deformation. These scale factors were determined based on the local station density and three-dimensional ground deformation. After this operation, the long-wavelength deformation caused by tectonic movement and small-scale deformation caused by human activities were separated.

Table 2. Geometric properties of the spherical–triangular grids [32].

Order, q	**Faces, F_q**	**Vertices, V_q**	**Average Side Arc-Length,** [a] $\bar{L}_q$		**Max Representable Bandwidth, $\bar{l}_q$**
0	20	12	63.435°	7053.64 km	3
1	80	42	31.718°	3526.82 km	6
2	320	162	15.859°	1763.41 km	11
3	1280	642	7.929°	881.71 km	23
4	5120	2562	3.965°	440.85 km	45
5	20,480	10,242	1.982°	220.43 km	91
6	81,920	40,962	0.991°	110.21 km	182
7	327,680	163,842	0.496°	55.11 km	363
8	1,310,720	655,362	0.248°	27.55 km	726
9	5,242,880	2,621,442	0.124°	13.78 km	1453
10	20,917,520	10,485,762	0.062°	6.89 km	2906
11	83,886,080	41,943,042	0.031°	3.44 km	5811
12	335,544,320	167,772,162	0.016°	1.72 km	11,623
q	$F_q = 20 \times 4^q$	$V_q = 10 \times 4^q + 2$	$\bar{L}_q = 2^{-q}\bar{L}_0$		$\bar{l}_q = int(\pi/\bar{L}_q)$

[a] $\bar{L}_0 = cos^{-1}\{\cos(72°)/[1-\cos(72°)]\} \approx 1.1071 \approx 63.43°$.

3.4. Inversion of Slip Rate and Locking Depth along the Weihe Fault

The cumulative seismic moment was directly related to the fault slip rate, locking depth, and fault length [33]. The accumulated seismic energy will increase with the locking depth and slip rate of the fault when the accumulation time and fault length are fixed.

Therefore, the slip rate and locking depth are two important parameters for assessing the seismic hazard and tectonic activity of an active fault [34]. Velocity profiles can provide direct observations to determine the slip rate and locking depth. In this study, a series of fault-perpendicular profiles (6 km wide and 20 km long) from the secular vertical velocity field after wavelet decomposition was extracted to invert the slip rate and locking depth. Taking into account the minimal horizontal movement in the study area, an improved dip-slip model was used to investigate the current slip rate and locking depth of the Weihe Fault [35]. The mathematical expression of the improved dip-slip model is shown as follows:

$$u_z = -\frac{s}{\pi}\left\{ \sin\delta \tan^{-1}\left[\frac{\left(x-\frac{d}{\tan\delta}\right)}{d}\right] + \frac{\cos\delta + \frac{\left(x-\frac{d}{\tan\delta}\right)}{d}\sin\delta}{1+\left[\frac{\left(x-\frac{d}{\tan\delta}\right)}{d}\right]^2} \right\} \tag{2}$$

where s is the relative slip rate between the hangingwall and footwall, u_z is the vertical slip rate, x is the distance from the observation point to the fault, d is the locking depth, and δ is the dip. Figure 3 shows the geometry of the dip-slip fault.

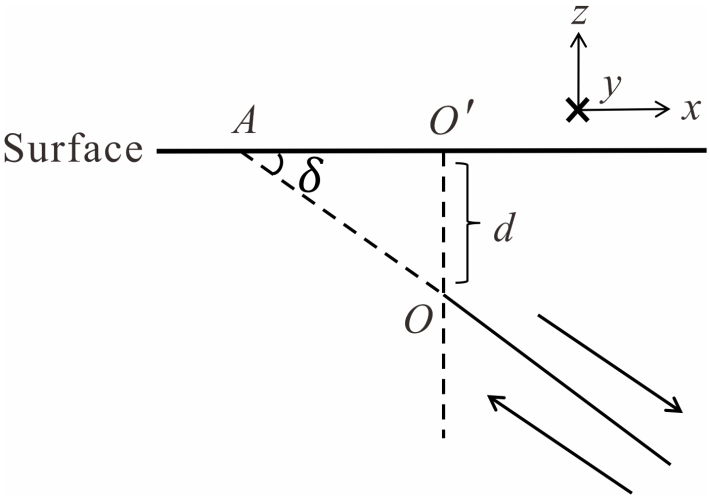

Figure 3. Displacement diagram of dip-slip fault.

4. Experiment and Analysis

4.1. LOS Deformation Rate from Stacking-InSAR

The LOS deformation rate of Weihe Faults was derived from stacking-InSAR technology using the collected Sentinel-1A images, as shown in Figure 4. All measurement values are relative to a common reference point (the red cross in Figure 4) that is considered to be stable over the entire time period. The positive and negative values indicated that the ground object was approaching and away from the satellite along the LOS direction, respectively. It is observed that the deformation presents a clear spatial pattern: the south of the Weihe Fault is mainly dominated by negative values, while the north is mainly dominated by the positive values. The maximum deformation is about 6.8 mm/yr, which is located at the north-west of Figure 4. The minimum deformation is about −8.2 mm/yr, which is located at the center-south of Figure 4. The LOS deformation is a combination of east–west, north–south and vertical components. It is possible to separate these components from LOS deformation if multi-platform SAR images with different orbital directions are collected, such as ALOS-2, TerraSAR-X and COSMO-SkyMed. However, it is difficult to separate these components in this case since only Sentinal-1A ascending images were involved in the deformation estimation. As indicated in a previous study, the Weihe Fault is dominated by the vertical deformation and slight strike-slip shear movement. Therefore, it is speculated that the LOS deformation rate estimated by stacking-InSAR in Figure 4 is mainly from the vertical component due to the fault and human activities.

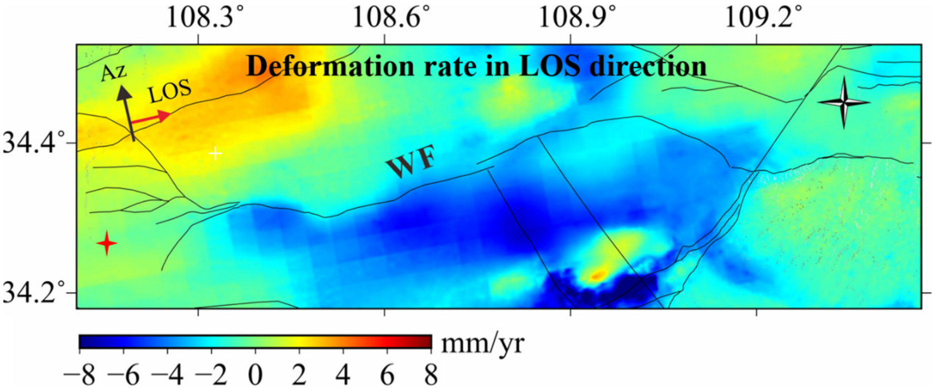

Figure 4. InSAR-derived deformation rate of the Weihe Fault, where the red cross represents the reference point.

4.2. Three-Dimensional Deformation Rates along the Weihe Fault

In order to obtain the east–west, north–south and vertical deformation components, the three-dimensional rates were calculated by integrating GNSS and InSAR observations, as described in Section 3.2, and as shown in Figure 5. The north–south components were mainly contributed to by GNSS data as the InSAR is insensitive to the north–south motion of its near-polar-orbit observations. It is found that deformation patterns in horizontal east–west (Figure 5a) and north–south directions (Figure 5b) are not as clear as the vertical deformation patterns (Figure 5c) in the Weihe Basin. The east–west deformation, ranging from 5.6 mm/yr to 7.4 mm/yr, is dominated by the eastern component. The north–south deformation, ranging from −3.2 mm/yr to −2.4 mm/yr, is dominated by the southern component. The small spatial variations in east–west and north–south deformation suggest the small strike-slip motion rate of the Weihe Fault. The spatial variations of vertical deformation (Figure 5c) are relatively large along the Weihe Fault, where the minimum and maximum deformation rates are −9.7 mm/yr and 6.2 mm/yr, respectively. There are two main reasons to explain it. The first is the activity of normal faults in the Weihe Basin, and the second is related to anthropological activities such as groundwater extraction and recharge. Precise leveling data are used to evaluate the integrated vertical deformation rates. As shown by the gray arrows in Figure 5c, they show the similar spatial pattern: subsidence in the south and uplift in the north. The statistical results show that the standard deviation between them is 1.69 mm/yr and the mean value is 0.6 mm/y, demonstrating the reliability of the produced vertical deformation.

4.3. Tectonic Deformation along Weihe Fault

The vertical deformation from the last section was decomposed by wavelet analyses to distinguish the long-wavelength tectonic movement and small-scale human-activities-induced deformation, as shown in Figure 6. It can be seen that the deformation fields decomposed by different scale factors manifested clear differences. The deformations composed with small-scale factors generally presented large-scale tectonic deformation characteristics, while deformation fields composed of large-scale factors were mainly from the non-tectonic deformation. As analyzed in Section 3.3, q = 5–10 was used as the secular vertical tectonic deformation (Figure 6d) and q = 11–12 was used as the local human-activities-induced deformation (Figure 6f). The estimated vertical field in Figure 6d reveals that the deformation on both sides of the Weihe Fault exhibit completely different patterns: the northern side is uplifting and the southern side is undergoing subsidence. The largest uplift area is located in Liquan county with a magnitude up to ~4.5 mm/yr, and the largest subsidence area is located to the south of the Weihe Fault with a magnitude up to

~6 mm/yr. Meanwhile, it can be seen in Figure 6d that the Weihe Fault exhibits the obvious vertical velocity gradient, implying stress accumulation and posing a risk of moderate to strong earthquakes in the Weihe Fault. The residual deformation (Figure 6f) reveals a spatial pattern dominated by strong subsidence or uplift signals, which are mainly caused by anthropogenic activities.

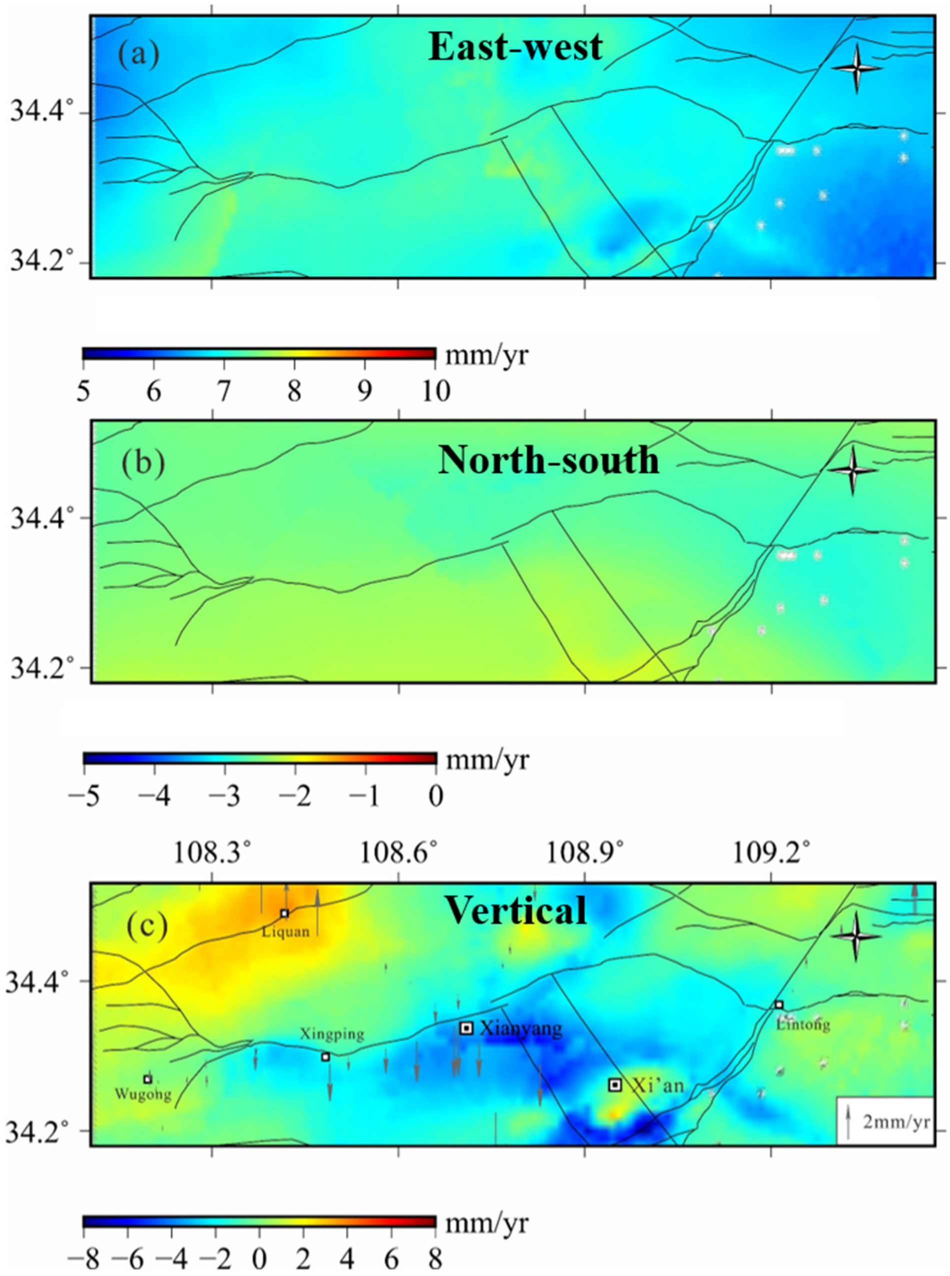

Figure 5. (**a**) East–west, (**b**) north–south and (**c**) vertical deformation rates through the integration of GNSS and InSAR observations. The gray arrows represent the leveling observations; the gray lines represent the faults; the black rectangle represent the location of cities.

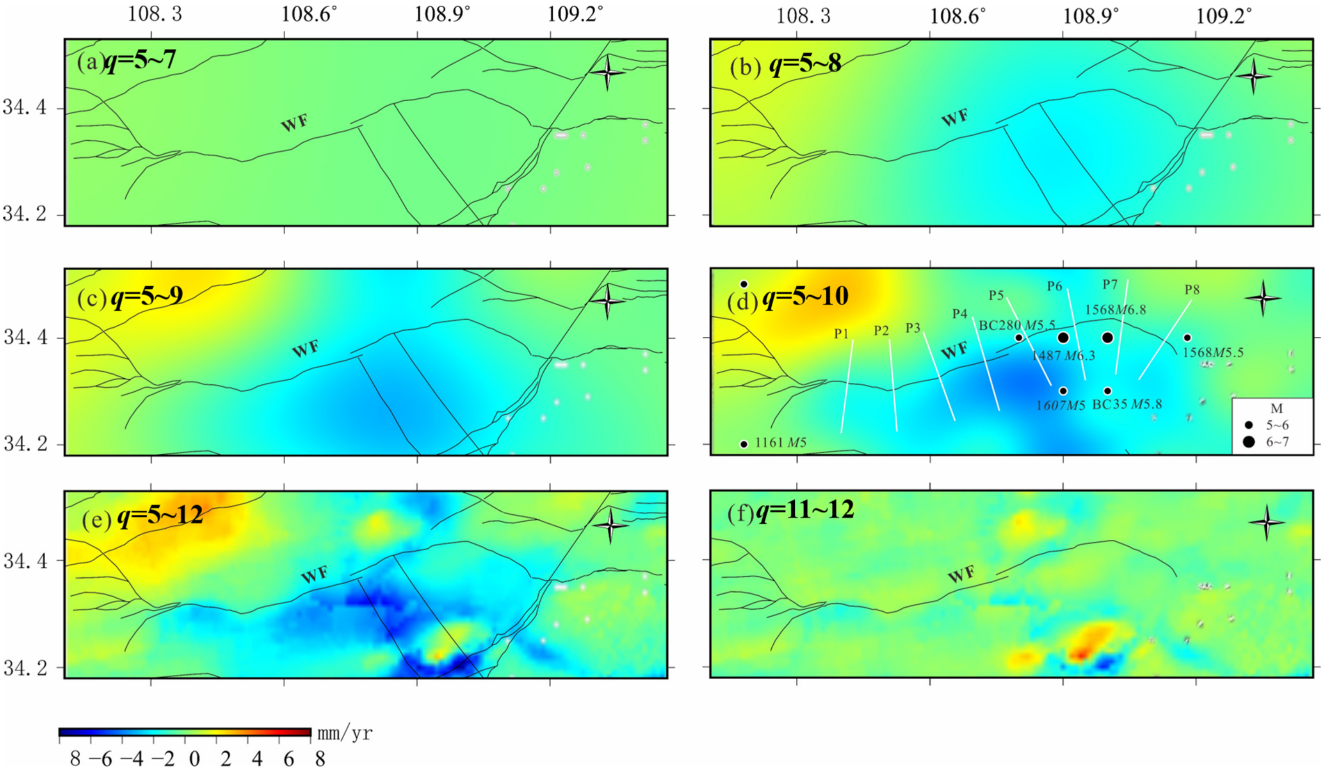

Figure 6. Multiscale vertical velocity field, using scales (**a**) q = 5–7, (**b**) q = 5–8, (**c**) q = 5–9, (**d**) q = 5–10, (**e**) q = 5–12, (**f**) q = 11–12. The white lines in (**d**) represent locations of profiles.

5. Discussion

5.1. Current Earthquake Risk of the Weihe Fault

To evaluate the earthquakes risk of the Weihe Fault, the variations of slip rate and locking depth along the profiles in Figure 6d were inverted by the improved dip-slip model, as shown in Figure 7. Gray dots and red lines in Figure 7 are secular vertical observations and the corresponding best-fitting models, and the best-fitting parameters (S, d and δ) are labeled on each subfigure. It can be seen that most observations are well fitted by the improved dip-slip model. The slip rate of the Weihe Fault shows a decreasing trend from west (~4 mm/yr) to east (~3 mm/yr), suggesting different activities at different sections of the Weihe Fault. This finding is consistent with prior research. However, the slip rate obtained in this study is higher than that of the geological results, which may be caused by the fact that the slip rate obtained by the geological method spans multiple seismic cycles while the rate obtained by the geodetic method is the current crustal deformation rate. The dip of the Weihe Fault is generally increasing from west (~50°) to east (~80°), which is slightly smaller than the previous results in the western section (65~80°) and slightly larger than those in the eastern section (70°). This difference may be related to the fact that the Weihe Fault is a shovel-type fault with a large dip in the shallow part (within 5 km) and a gradually smaller dip in the deeper part, while the dip-slip model used in this study did not consider the variation of the fault dip with different depths. For the locking depth, the results showed that the locking depth was gradually increasing from west (~5 km) to east (~14 km). It should be noted that the locking depth for profile 6 was very large, indicating that the slip rate in this profile was not significant.

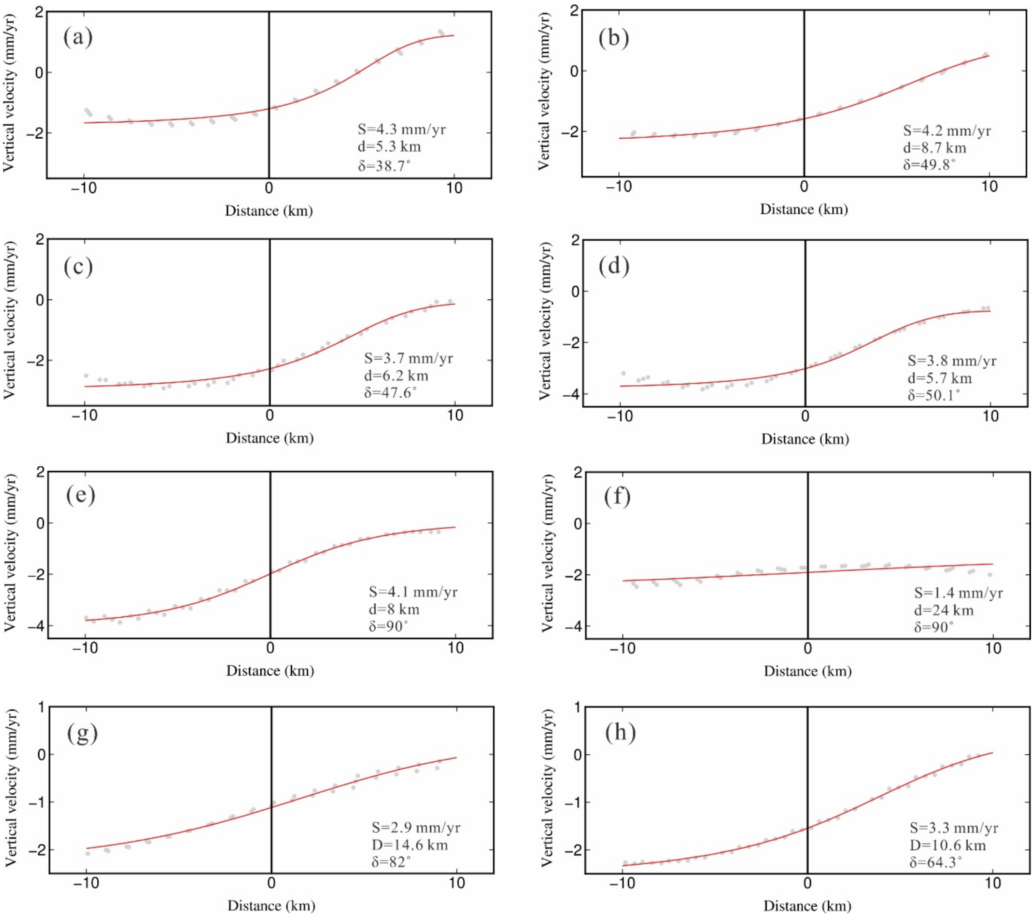

Figure 7. The vertical velocity along profile lines P1 (**a**), P2 (**b**), P3 (**c**), P4 (**d**), P5 (**e**), P6 (**f**), P7 (**g**) and P8 (**h**) marked in Figure 6d. Gray dots and red lines are secular vertical observations and the corresponding best-fitting models, respectively. The best-fitting model parameters are labeled on each figure.

According to the earthquake catalogues of the Weihe Fault, most earthquakes are distributed on the eastern section of the Weihe Fault, including the 1161 M5, 280 BC M5.5, 1487 M6.3, and the 1568 M6.8 events. Taking into account the higher locking depth and historical earthquake record, attention should be paid to the earthquake risk of the eastern section of the Weihe Fault.

5.2. Ground Subsidence Caused by Groundwater Withdrawal

The residual small-scale deformation (Figure 6f) obtained by the wavelet analysis shows the clear local deformation funnels, which are mainly related to the excessive exploitation of groundwater [14]. The activities of normal faults in the Weihe Basin resulted in the accumulation of a thick pile of sediments in the rift basin. The thickness of the Quaternary strata in the Weihe Basin could reach 600 to 1000 m, with a shallow depth within 300 m, mainly composed of cohesive soil [16]. It is known that irreversible plastic deformation will occur for the cohesive soil when releasing water pressure. Therefore, the overexploitation of groundwater can easily cause ground subsidence in the Weihe Basin. Furthermore, the existence of the Weihe Fault disrupts the integrity of groundwater flows and limits the lateral extent of the subsidence. In addition to subsidence, uplift deformation with a rate up to ~5 mm/yr is also observed in the study area, which may be related to the recharge of urban groundwater [2].

6. Conclusions

To investigate the activity of the Weihe Fault, three-dimensional ground deformation rates were estimated by the integration of GNSS and InSAR observations, and the vertical component was evaluated by using the dependently observed leveling data. Then, the tectonic vertical deformation was decomposed from the integrated vertical deformation field by wavelet analysis. Finally, the improved dip-slip model was adopted to inverse the slip rate, locking depth, and dip changes along the Weihe fault. Based on this study, the following conclusions are made:

(1) The high-spatial-resolution vertical deformation rate of the Weihe Fault was successfully estimated through integrating InSAR and GNSS observations. The GNSS was sensitive to the horizontal deformation, while InSAR was sensitive to the vertical deformation. Based on this fact, the three-dimensional deformation rates were produced by integrating GNSS and InSAR datasets. The standard deviation between the leveling and integrated vertical deformation rate was 1.69 mm/yr, and the mean value was 0.6 mm/yr, demonstrating the reliability of the proposed method.

(2) The earthquake risk of the eastern section of the Weihe Fault should attract attention. The long-wavelength tectonic movement and small-scale human-activities-induced deformation were decomposed by wavelet analyses. The expected tectonic velocity gradient was found along the Weihe Fault, implying stress accumulation and posing a risk of moderate to strong earthquakes in the Weihe Fault. Taking into account the higher locking depth and historical earthquake record, attention should be paid to the earthquake risk of the eastern section of the Weihe Fault.

Although the activity of the Weihe Fault was investigated in this study, there are still two limitations. The first concerns the limited SAR images. A total of 26 ascending Sentinel-1A images spanning from 2015 to 2019 were utilized in this case. These datasets may be enough for estimating the LOS deformation rate. However, they are not enough to obtain the two- or three-dimensional time series deformation. The second limitation concerns the time series deformation. Besides spatial deformation variation, temporal deformation variation is also an important aspect of fault investigation. However, the time series deformation in the Weihe Fault was not estimated in this study due to the limited datasets. Thus, these two limitations should be addressed in the future.

Author Contributions: Conceptualization, Q.-H.T. and W.-T.Z.; methodology, Q.-H.T., W.-T.Z. and W.Z.; software, Q.-H.T., W.-T.Z. and W.Z.; validation, Q.-H.T. and W.-T.Z.; formal analysis, Q.-H.T., W.-T.Z. and W.Z.; investigation, W.-T.Z. and W.Z.; resources, Q.-H.T. and W.-T.Z.; data curation, Q.-H.T., W.-T.Z. and W.Z.; writing—original draft preparation, Q.-H.T.; writing—review and editing, W.-T.Z. and W.Z.; visualization, Q.-H.T., W.-T.Z. and W.Z.; supervision, W.Z.; project administration, W.-T.Z.; funding acquisition, Q.-H.T. and W.Z. All authors have read and agreed to the published version of the manuscript.

Funding: This research was funded by the Natural Science Foundation of China (NSFC) (Nos. 42074040, 42004048), Natural Science Basic Research Plan in Shaanxi Province of China (2023-JC-JQ-24), Key Research and Development Program of Shaanxi (No. 2021ZDLSF06-02), Innovative Talents Promotion Plan of Shaanxi Province (Grant No. 2022KJXX-22), and Fundamental Research Funds for the Central Universities of CHD (Nos: 300102262902, 300102263401, 300102262512).

Institutional Review Board Statement: Not applicable.

Informed Consent Statement: Not applicable.

Data Availability Statement: Not applicable.

Acknowledgments: Several figures were prepared using Generic Mapping Tools software. We are grateful to the anonymous reviewers for their constructive comments that improved this manuscript.

Conflicts of Interest: The authors declare no conflict of interest.

References

1. Deng, W.; Song, J.; Sun, H.; Cheng, D.; Zhang, X.; Liu, J.; Kong, F.; Wang, H.; Khan, A.J. Isolating of climate and land surface contribution to basin runoff variability: A case study from the Weihe River Basin, China. *Ecol. Eng.* **2020**, *153*, 105904. [CrossRef]
2. Qu, F.; Zhang, Q.; Niu, Y.; Lu, Z.; Wang, S.; Zhao, C.; Zhu, W.; Qu, W.; Yang, C. Mapping the recent vertical crustal deformation of the Weihe Basin (China) using Sentinel-1 and ALOS-2 ScanSAR imagery. *Remote Sens.* **2022**, *14*, 3182. [CrossRef]
3. Yang, C.; Ji, L.; Yang, Y.; Su, L.; Wang, Y.; Shi, H. Present-day activity and seismic potential of the north Qinling fault, southern ordos block, central China, as revealed from GPS data and seismicity. *Front. Earth Sci.* **2023**, *10*, 2396. [CrossRef]
4. Peng, J.B. Tectonic evolution and seismicity of Weihe Fault zone. *Seismol. Geol.* **1992**, *14*, 113–120.
5. Luo, Q.; Li, C.; Ren, G.; Hu, X.; Li, X.; Li, Y. The 1673 Tianzhen earthquake and rupture behavior of the Yanggao-Tianzhen Fault in the northern Shanxi Graben, China. *Tectonics* **2023**, *42*, e2022TC007582. [CrossRef]
6. Ren, J.; Peng, J.B.; Wang, F.Y.; Liu, C.; Feng, X.J.; Dai, W.Q. The research of deep structural features of Weihe basin and adjacent areas. *Chin. J. Geophys.* **2012**, *55*, 2939–2947.
7. Zhang, Y.Z.; Xu, H.J.; Wang, W.D.; Liu, J.; Shan, F. Inversion on Slip Velocity of Main Faults in Weihe Basin by Particle Swarm Optimization Algorithm with GPS Data. *China Earthq. Eng. J.* **2011**, *33*, 322–325.
8. Zhang, Q.; Qu, W.; Peng, J.B.; Wang, Q.L.; Li, Z.H. Research on tectonic causes of numerous ground fissures development mechanism and its unbalance distribution between eastern and western of Weihe basin. *Chin. J. Geophys.* **2012**, *55*, 2589–2597.
9. Hu, Y.; Qin, S.; Hao, M. Three-dimensional crustal deformation before and after the Wenchuan earthquake in Guanzhong and adjacent regions. *Geod. Geodyn.* **2015**, *6*, 16–24. [CrossRef]
10. Qu, W.; Wang, Y.S.; Xu, C.; Zhang, Q.; Wang, Q.L. Current Tectonic Stress and Activities Characteristics of the Deep Faults Within Weihe Basin. *Geomat. Inf. Sci. Wuhan Univ.* **2017**, *42*, 825–830.
11. Cui, D.X.; Hao, M.; Qin, S.L.; Wang, W.P. Inversion of fault dip-slip rate and locking depth in Central-Southern Shaanxi of China. *Chin. J. Geophys.* **2019**, *62*, 4648–4657.
12. Gao, Y.; Qu, W.; Zhang, Q.; Wang, Q.L.; Hao, M. Differential Characteristics of Present-Day Crustal Movement and Strain Field in the Fenwei Basin and Its Surrounding Regions Revealed by GNSS Observations. *Geomat. Inf. Sci. Wuhan Univ.* **2021**, *46*, 1063–1070.
13. Cai, X.C.; Tang, H.T. Discussion on dynamic evolution characteristics of the crust in the southwestern margin of Ordos block based on GPS data. *Seismol. Geomagn. Obs. Res.* **2022**, *43*, 14–21.
14. Peng, M.; Zhao, C.; Zhang, Q.; Lu, Z.; Li, Z. Research on spatiotemporal land deformation (2012–2018) over Xi'an, China, with multi-sensor SAR datasets. *Remote Sens.* **2019**, *11*, 664. [CrossRef]
15. Chen, J.; Zhang, D.L.; Zhou, Y. Estimating present slip rate of the faults in the Weihe Graben using Envisat ASAR data. *Seismol. Geol.* **2020**, *42*, 333–345.
16. Niu, Y.F. Applications of SAR interferometry for co-seismic, interseismic and volcano deformation monitoring, modeling and interpretation. *Acta Geod. Cartogr. Sin.* **2022**, *51*, 471.
17. Li, X.N.; Zhang, P.Z.; Zheng, W.J.; Feng, X.J.; Li, C.Y.; Pierce, I.K.; Xu, H.Y. Kinematics of Late Quaternary Slip Along the Qishan-Mazhao Fault: Implications for Tectonic Deformation on the Southwestern Ordos, China. *Tectonics* **2018**, *37*, 2983–3000. [CrossRef]
18. Du, J.; Shi, C.X. Effects of climatic factors and human activities on runoff of the Weihe River in recent decades. *Quatern. Int.* **2012**, *282*, 58–65. [CrossRef]
19. Peng, J.B.; Su, S.R.; Mi, F.S. *Active Faults and Geological Hazards in the Weihe Basin*; Northwest University Press: Evanston, IL, USA, 1992.
20. Yang, C.; Li, X.; Tao, W. Microstructure characteristics and tectonic significance of bedrock fault plane of the Kouzhen-Guanshan fault. In *Advances in Geology and Resources Exploration*; CRC Press: Boca Raton, FL, USA, 2022; pp. 88–96.
21. Du, J.; Li, D.; Wang, Y.; Ma, Y. Late quaternary activity of the Huashan Piedmont fault and associated hazards in the southeastern Weihe Graben, Central China. *Acta Geol. Sin. Engl. Ed.* **2017**, *91*, 76–92. [CrossRef]
22. Li, W.; Feng, X. Discovery of the Qinghe fault, the inner part of the Weihe graben, central China, and its geological significance. *Front. Earth Sci.* **2023**, *11*, 1127897. [CrossRef]
23. Wang, M.; Shen, Z.K. Present-day crustal deformation of continental China derived from GPS and its tectonic implications. *J. Geophys. Res.* **2020**, *125*, e2019JB018774. [CrossRef]
24. Hao, M.; Wang, Q.; Cui, D.; Liu, L.; Zhou, L. Present-day crustal vertical motion around the Ordos block constrained by precise leveling and GPS data. *Surv. Geophys.* **2016**, *37*, 923–936. [CrossRef]
25. Sandwell, D.T.; Price, E.J. Phase gradient approach to stacking interferograms. *J. Geophys. Res.* **1998**, *103*, 30183–30204. [CrossRef]
26. Zhang, W.T.; Zhu, W.; Tian, X.D.; Zhang, Q.; Zhao, C.; Niu, Y.F.; Wang, C.S. Improved DEM Reconstruction Method based on Multi Baseline InSAR. *IEEE Trans. Geosci. Remote Sens. Lett.* **2022**, *19*, 4011505.
27. Costantini, M. A novel phase unwrapping method based on network programming. *IEEE Trans. Geosci. Remote Sens.* **1998**, *36*, 813–821. [CrossRef]
28. Ferretti, A. Nonlinear subsidence rate estimation using permanent scatters in differential SAR interferometry. *IEEE Trans. Geosci. Remote Sens.* **2000**, *38*, 2202–2212. [CrossRef]
29. Weiss, J.R.; Walters, R.J.; Morishita, Y.; Wright, T.J.; Lazecky, M.; Wang, H.; Parsons, B. High-resolution surface velocities and strain for Anatolia from Sentinel-1 InSAR and GNSS data. *Geophys. Res. Lett.* **2020**, *47*, e2020GL087376. [CrossRef]

30. Shen, Z.K.; Liu, Z. Integration of GPS and InSAR data for resolving 3-dimensional crustal deformation. *Earth Space Sci.* **2020**, *7*, e2019EA001036. [CrossRef]
31. Shen, Z.K.; Wang, M.; Zeng, Y.; Wang, F. Optimal interpolation of spatially discretized geodetic data. *B Seismol. Soc. Am.* **2015**, *105*, 2117–2127. [CrossRef]
32. Tape, C.; Musé, P.; Simons, M.; Dong, D.; Webb, F. Multiscale estimation of GPS velocity fields. *Geophys. J. Int.* **2009**, *179*, 945–971. [CrossRef]
33. Savage, J.C.; Burford, R.O. Geodetic determination of relative plate motion in central California. *J. Geophys. Res.* **1973**, *78*, 832–845. [CrossRef]
34. Joshi, M.; Naik, S.P.; Mohanty, A.; Bhadran, A.; Girishbai, D.; Ghosh, S. First hand observations from the April 28, 2021 Sonitpur (MW 6.4) earthquake, Assam, India: Possible mechanism involved in the occurrence of widespread ground effects. *Geosci. J.* **2023**, *27*, 225–239. [CrossRef]
35. Zou, Z.Y.; Jiang, Z.S.; Wu, Y.Q.; Wei, W.X.; Liu, X.X.; Zhang, L. Improvements for the strike/Dip-slip displacement theory formula of general dip fault. *J. Geod. Geodyn.* **2015**, *35*, 460–468.